

# Analysis of the UH-60A Rotor Loads Using Wind Tunnel Data

Ritu P. Marpu<sup>1</sup> and Lakshmi N. Sankar<sup>2</sup>

*School of Aerospace Engineering, Georgia Institute of Technology, Atlanta, GA, 30332-0150*

Thomas R. Norman<sup>3</sup>

*Flight Vehicle Research and Technology Division, NASA Ames Research Center, Moffett Field, CA, 94035*

T. Alan Egolf<sup>4</sup> and Stephen Makinen<sup>5</sup>

*Sikorsky Aircraft Corporation, Stratford, CT, 06614*

A subset of the US-Army/NASA wind tunnel tests of a full-scale UH-60A Black-Hawk rotor system are studied using a Hybrid Navier-Stokes Free-Wake Computational Fluid Dynamics methodology, coupled with a multi-body dynamics analysis code. A speed sweep at constant lift for advance ratios ranging between 0.15 and 0.37 and a thrust sweep at constant advance ratio ranging from no stall to deep stall conditions are investigated. Results are presented for sectional airloads, structural loads and integrated forces and moments at the hub. There is reasonable agreement between measured and predicted performance indicators such as thrust and power for the parametric speed and the thrust sweeps, while the propulsive force is over-predicted. The lift to equivalent drag ratio is slightly under-predicted for both the parametric sweep conditions. The predicted trim settings are consistent with measurements.

## Nomenclature

$\mu$	=	advance ratio
$M_{tip}$	=	tip Mach number
$C_L$	=	rotor lift coefficient
$C_P$	=	power coefficient
$C_T$	=	rotor thrust coefficient
$C_X$	=	propulsive force coefficient
$L/D_e$	=	lift to equivalent drag ratio = $C_L / (C_P/\mu - C_X)$
$\alpha_s$	=	shaft angle of attack
$\alpha_c$	=	shaft angle of attack corrected for wind tunnel wall corrections
$\sigma$	=	solidity
$C_n M^2$	=	sectional normal loads, nondim. by $\frac{1}{2} \rho a^2 c$
$C_m M^2$	=	sectional pitching moments, nondim. by $\frac{1}{2} \rho a^2 c^2$

## I. Introduction

THE prediction of rotorcraft aeromechanics is a challenging task due to the complex environment that the rotor blades operate under. Rotors in forward flight experience a wide range of aerodynamic phenomena including the bundling of vortices at low speeds, transonic effects at high speeds and dynamic stall phenomena at high thrust

---

<sup>1</sup> PhD Candidate, School of Aerospace Engineering, Georgia Institute of Technology, and AIAA Student Member.

<sup>2</sup> Regents Professor, School of Aerospace Engineering, Georgia Institute of Technology, and AIAA Member.

<sup>3</sup> Aerospace Engineer, Flight Vehicle Research and Technology Division, NASA Ames Research Center.

<sup>4</sup> Supervisor, Aerodynamic Methodology, Sikorsky Aircraft Methodology and AIAA Member.

<sup>5</sup> Senior Engineer/Flight Sciences Technical Lead, Dynamics and Internal Acoustics, Sikorsky Aircraft Corporation and AIAA Member

conditions. Helicopters at low speed transition flight and high speed flights experience significant vibration. From a rotorcraft designer's perspective, accurate prediction of mean and peak-to-peak loads is not adequate to size the expensive rotor hub components. The harmonic content of loads in the rotating system is crucial for capturing peak-to-peak loads in the fixed system. For example, the 4P swash-plate servo loads (fixed system) are dependent upon the 3-5P pushrod loads (rotating system). Therefore, the next generation rotorcraft predictive tools must be equipped to accurately predict the mean, peak-to-peak as well as harmonic content of structural and aerodynamic loads. In addition, performance indicators such as power, propulsive force, lift to drag ratio etc, must be captured accurately by these tools.

Validation of these next generation predictive tools requires high quality experimental data. The NASA-Army UH-60A Airloads Program<sup>1</sup> provides one such database, consisting of flight test data that includes pilot input, vehicle attitudes, blade airloads and structural loads. A number of steady and maneuvering flight counters were flown as a part of this program. Significant research has been done in the past decade to understand the fundamental phenomena underlying the steady flight conditions.<sup>6-9</sup> The present researchers have used this flight test database to study the UH-60A rotor under steady level flight conditions<sup>4,10,12</sup> and transient maneuvers – UTTAS pull-up maneuver 11029, and diving turn maneuvers 11680 and 11679.<sup>13-14</sup> While steady and maneuvering flight test data provide a valuable resource for validating rotorcraft aeromechanical predictive tools, they are coupled with vehicle dynamics and pilot control inputs and contain uncertainties associated with recording flight test data. In order to address these limitations with flight test data, a controlled set of high quality wind tunnel data for the UH-60A configuration was recently conducted.<sup>2</sup>

NASA and the US Army have completed (May 2010) a wind tunnel test on a full-scale pressure-instrumented UH-60A rotor system at the USAF's National Full-Scale Aerodynamics Complex 40- by 80-Foot Wind Tunnel. The primary objective of this NASA/Army test program was to provide an extensive database for the validation of predictive tools.<sup>2,15</sup> A variety of flight conditions were studied, including speed sweeps at constant thrust (for advance ratios up to 0.4) and thrust sweeps at a constant advance ratio. The data acquired from this test included blade airloads and structural loads, steady and oscillatory hub forces and moments, and blade displacements and deformations. Romander et al.,<sup>15</sup> investigated specific parametric speed and thrust sweeps by employing loosely coupled OVERFLOW and CAMRAD II and obtained detailed airloads and performance data. Yeo et al.,<sup>16</sup> investigated the quality of aeromechanical load prediction for the speed and thrust sweeps using two approaches – comprehensive analysis only (CAMRAD II) and CFD/CSD (CAMRAD II/OVERFLOW 2) and reported significant improvement in predictions using the coupled CFD/CSD analysis.

In the current study, the full-scale wind tunnel data for the UH-60A rotor<sup>2</sup> will be used to compare measured rotor airloads, structural loads and performance indicators with predictions. In this study, two parametric sweeps will be investigated. The first parametric sweep study consists of a range of advance ratios,  $\mu = 0.15$  to  $0.4$ , at constant lift ( $C_L/\sigma = 0.09$ ) and constant tip Mach number of  $0.65$ . The second study consists of a thrust sweep from a lightly loaded rotor through deep stall conditions, at a constant advance ratio ( $\mu = 0.3$ ) and a constant tip Mach number of  $0.625$ . The aim of the current study is to utilize the high-quality wind tunnel data to further validate the present computational methodology without uncertainties associated with the flight test data.

## II. Computational Methodology

### A. CFD Methodology

The CFD methodology used in this study is GT-Hybrid.<sup>4</sup> GT-Hybrid is a three-dimensional unsteady viscous compressible flow solver. The flow is modeled by first principles using the Navier-Stokes Methodology. GT-Hybrid solves the three-dimensional unsteady Navier-Stokes equations in the transformed body-fitted coordinate system using a time-accurate, finite volume scheme. A third-order spatially accurate Roe scheme is used for computing the inviscid fluxes and a second order central differencing scheme is used for viscous terms. The Navier-Stokes equations are integrated in time by means of an approximate LU-SGS implicit time marching scheme. The flow is assumed to be turbulent everywhere, and hence no transition model is currently used. The solver accepts a user defined table of blade geometric and elastic deformations and deforms the computational grid. The temporal change in computational cell volume is accounted for by explicitly satisfying the Geometric Conservation Law (GCL). GT-Hybrid currently has the capability to use advanced turbulence models such as SA-DES and KES to compute the eddy viscosity.

GT-Hybrid CFD solver utilizes a hybrid methodology where the flow field near the blade is resolved through the Navier-Stokes solution, whereas the influence of the other blades and of the trailing and shed vorticity in the far field wake are accounted for by modeling them as a collection of piece-wise linear bound and wake vortex elements, as shown in Fig. 1. The near wake is captured inherently in the Navier-Stokes analysis. The use of such a hybrid

Navier-Stokes/vortex modeling method allows for an accurate and economical modeling of viscous features near the blades, and an accurate “non-diffusive” modeling of the wake in the far field.

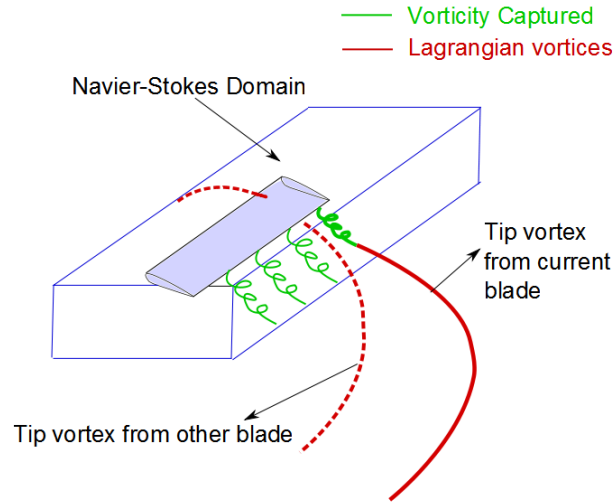


**Fig. 1. Schematic of Hybrid methodology.**

The vortex model is based on a Lagrangian wake approach where a collection of vortex elements are released from the rotor blade trailing edge and are convected downstream by a combination of the free-stream velocity and the bound and wake vortex element self-induced velocities. The strength of the vortex elements is based on the radial and temporal gradients of the bound circulation. The number of spanwise wake trailers and wake time step increment are chosen by the user. The influence of these vortices on the blade aerodynamics is computed by appropriately specifying the vortex-induced velocities at the far field boundary of the Navier-Stokes domain, neglecting the contribution of the elements within the CFD volume grid released from the blade. A schematic of the multiple wake trailer model is shown in Fig. 2.

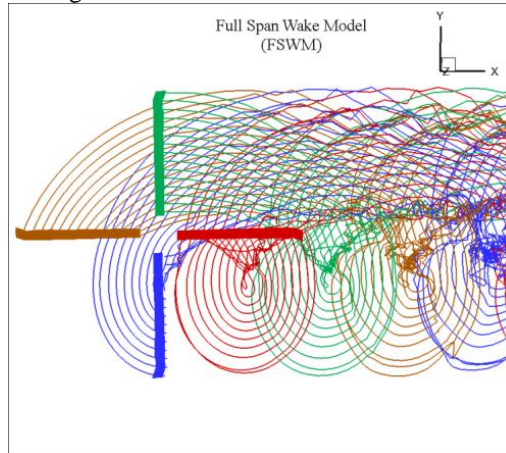


**Fig. 2. Multiple trailer representation of wake.**

## B. Computational grid

For this work, the computational grid over each blade has 131x65x45 nodes in chordwise, spanwise and normal directions respectively. The blade surface has 90 chordwise points and 50 spanwise points. The spanwise points are clustered towards the blade tip region. The CFD grid was generated from a CAD representation of the blade surface geometry. The far field boundary is located nine chords away from the blade surface. The normal grid spacing at the blade surface is about  $1.0^{-5}c$ , where  $c$  is the reference chord length. The grid is clustered near the tip and near the leading and trailing edges to handle regions of high gradients. The grid is based on a C-H grid topology.

### C. DYMORE CSD Methodology

DYMORE<sup>5</sup> is a computational structural dynamics (CSD) solver used in this study. It is a multi-body finite element code for arbitrary non-linear elastic systems. The multi-body models are constructed by connecting basic structural elements; the data for these elements are stored within an element library. Each of these elements has its own system of equations which when integrated create larger and more complex equations. The multibody code incorporates robust and efficient time integration algorithms for integrating the resulting large scale, nonlinear, differential or algebraic equations. The rotor blades are modeled as elastic beams with geometrically exact composite beam finite element formulation. Rotorcraft comprehensive analyses solvers typically include internal lifting line based aerodynamic model as well as auto-pilot algorithm which can be used to perform a fully trimmed aeroelastic simulation of an isolated rotor configuration. DYMORE has been used extensively by researchers for performing comprehensive analyses because of the in-built lifting line aerodynamics, non-linear inflow models as well as auto-pilot trimmer. DYMORE can be coupled to external CFD solver to perform aeroelastic computations. In the simulations presented in this study, a four bladed UH-60A rotor model is used. The model includes blade, lag damper, push rod, rotor hub and swash plate. A lifting line based 2-D table lookup aerodynamics with dynamic wake model is used for computing airloads internally.

### D. CFD/CSD Loose Coupling and Trim Methodology

The CFD solver (GT-Hybrid) and CSD solver (DYMORE) are externally coupled in a loosely coupled manner. The delta-trim algorithm or loose coupling procedure pioneered by Tung, Caradonna and Johnson<sup>3</sup> is used to obtain trim solution and convergence of the CFD/CSD coupled analyses. At the beginning of the coupling process, the comprehensive analysis computes the trim solution and blade dynamics by utilizing the internal lifting line aerodynamic solution. The computed elastic blade deformations are then given as input to the CFD solver which in turn solves for the flow-field, for an entire rotor revolution until convergence in flow-field data is obtained. This concludes the first CFD/CSD iteration. In the subsequent CFD/CSD coupling iterations, the difference between the CFD airloads and the lifting line airloads from the previous iteration, added to the lifting line solution for the current iteration comprise the total airloads seen by the comprehensive analysis for the current iteration. Thus, the total airloads within the comprehensive solver are incrementally replaced by the airloads predicted by external CFD code, in an iterative manner.<sup>6</sup>

$$F_0 = F_0^{LL}$$

$$F_n = F_n^{LL} + (F_{n-1}^{CFD} - F_{n-1}^{LL})$$

In the numerical predictions, the trim targets are specified in the CSD methodology (DYMORE) to be the measured rotor thrust ( $C_T/\sigma$ ), the measured hub moments, and the corrected shaft angle ( $\alpha_c$ ). The corrected shaft angle ( $\alpha_c$ ) was derived by applying a Prandtl-Glauert wall correction to the geometric shaft angle ( $\alpha_s$ ) (Ref. 2) to account for the effects of the tunnel walls. The hub moments were approximately zero for the thrust sweep and were non-zero for the speed sweep conditions (simulating a rotor in 1-g flight). The autopilot algorithm in DYMORE adjusts the collective and cyclic controls to match the specified trim targets.

## III. Parametric Speed Sweep

Numerical predictions have been obtained for a parametric speed sweep as tabulated in Table 1. All the speed sweep conditions were carried out at  $C_L/\sigma = 0.09$  and a constant tip Mach number  $M_{tip}$  of 0.625.

Run*	Data Point	Advance Ratio ( $\mu$ )	Corrected shaft angle of attack (deg)
52	15	0.15	0.89
52	20	0.20	-0.31
52	25	0.24	-1.50
52	31	0.30	-3.49
52	35	0.35	-5.58
52	40	0.37	-6.74

**Table 1. Wind-tunnel speed-sweep conditions at  $C_L/\sigma = 0.09$ . (Ref. 2)**

The sectional airloads (normal force and pitching moment) as well as the blade structural loads were studied for the parametric speed sweep run. In this section, the effects of increasing the advance ratio for the same value of non-dimensional lift will be discussed.

#### **A. Lowest Advance Ratio run (5215)**

The lowest advance ratio,  $\mu = 0.15$  presents a challenge to the Hybrid CFD methodology since there is occurrence of Blade Vortex Interaction (BVI) phenomena at this advance ratio. The effects of the near-wake are critical for capturing the BVI events accurately. Using the current Hybrid approach, the effects of the near wake elements are very diffused. Therefore, it is important to study how well the Hybrid methodology is able to predict airloads at this advance ratio. Since the advance ratio is low, the wake is not convected away from the blades quickly and remains in the plane of rotor rotation. The older vortices released from the blades convect above the rotor plane and interact with the flow over the subsequent blades to give rise to impulsive loading.

The sectional normal loads and pitching moments for this test condition are shown in Fig. 3. The trends in sectional normal force are well matched. The BVI phenomenon is sensitive to miss distance, vortex strength as well as crossing of the vortices. The high frequency impulsive loading characteristic of BVI events is evident in the sectional pitching moment data near  $\psi = 75^\circ$  and  $\psi = 270^\circ$  azimuthal locations. The impulsive behavior starts at  $r/R = 0.775$  and extends through the tip region. Although the agreement in the sectional normal loads is adequate, the pitching moment data misses peak-to-peak predictions.

The vortex trailer trajectories from  $r/R = 0.865$  to the tip region have been plotted in Fig. 4 colored according to the vortex strength. It can be seen that the strongest vortices are found near  $\psi = 270^\circ$ . In Fig. 5, the vortex crossings above and below the rotor tip path plane are shown. The vortices are colored according to their vicinity from the rotor tip path plane. The vortices trailed by the previous blade (shown at  $\psi = 0^\circ$  in Fig. 5) intersect the blade tip region of the successive blade at  $\psi = 270^\circ$ . Similar vortex crossings are seen at  $\psi = 90^\circ$ . The CFD predictions capture the BVI events reasonably well, although the peak-to-peak of the impulsive loading has not been well-captured by the hybrid CFD methodology.

The impulsive loading due to BVI is sensitive to wake modeling effects as the wake representation determines the induced inflow over the rotor disk. Therefore, the effect of using a single tip vortex representation vs. multiple trailing and shed vortices representation has been studied for this advance ratio. Results indicate that the inboard loading behavior in between 22.5% and 40% radial stations, is better captured using the multiple trailer wake in conjunction with the shed wake model. The multiple trailer wake model appears to better predict the strength and geometry of the inboard vortices. This in turn improves the induced velocity prediction over the rotor disk. In contrast, the single tip vortex model has been observed to over-predict the peak-to-peak magnitude of sectional airloads at all radial locations. It may be inferred that the vortices trailed from the in-board radial locations for this flight condition have a considerable effect on the blade loading.

#### **B. Blade root motion**

The time history of blade root motion from the converged CFD/CSD analysis was used to extract the collective, longitudinal and lateral cyclic control angles. These values are compared with the measured collective, longitudinal and lateral cyclic angles as shown in Figs 6 a-c. As the advance ratio increases, the propulsive power increases thereby resulting in an increase in the collective. With increase in advance ratio, the longitudinal cyclic is increased to counteract the increasing nose-down pitching moment thereby maintaining trim in the longitudinal direction. As shown in Figs 6 a-b, the collective and longitudinal cyclic compare well with the measured values for the parametric speed-sweep. However, there is a constant difference of 1-1.5 deg between measured and predicted lateral cyclic angles, as seen in Fig. 6 c.

#### **C. Sectional Airloads**

The effects of increasing the advance ratio for a constant tip Mach number were studied for the conditions enlisted in Table 1. For the low advance ratio cases runs 5215 and 5220, the CFD solution required a larger number of rotor revolutions within the coupling process for achieving convergence of the rotor hub loads. The contribution of induced inflow towards the blade sectional angle of attack is higher at lower advance ratios. Therefore, it takes a larger number of rotor revolutions for the wake induced loads to attain steady state solution.

A qualitative representation of the predicted sectional normal loads and pitching moments for 3 advance ratios  $\mu = 0.15, 0.3$  and  $0.37$  is shown in Fig. 7. The pitching moments data in Fig. 7 a, shows impulsive loading in the first and fourth quadrant due to the occurrence of BVI phenomena. Sectional normal loads in Figs 7 b and c corresponding to  $\mu = 0.3$  and  $0.37$ , depict negative loading on the advancing side tip region, which is produced to accommodate roll moment balance in high speed flight. The negative normal loads at the inboard stations on the

retreating side are also seen due to reverse flow. Similarly the pitching moment data in Figs 7 b and c show negative moments on the advancing side, which is characteristic of high speed flight.

A detailed comparison of sectional normal loads and pitching moments near the tip region  $r/R = 0.92$ , at the same advance ratios  $\mu = 0.15, 0.3$  and  $0.37$  is shown in Fig. 8. On the advancing blade, transonic flow sets in at the tip region, causing negative lift at the end of the first quadrant. With increase in advance ratio, the negative loading in the blade sectional normal loads becomes more pronounced as compressibility effects intensify. Increased nose down pitching moments are observed as well. The CFD/CSD predictions show an under-prediction in peak-to-peak magnitude of pitching moments.

#### D. Structural Loads

The blade structural loads namely the flapwise bending moment, torsional moment and edgewise bending moment at 40%R have been compared in Fig. 9 for advance ratios of 0.15, 0.3, and 0.37. Steady values have been removed from the measured and predicted data. The waveform of the flapwise bending moments follows the waveform of the normal loads data. At  $\mu = 0.15$ , there are two troughs observed in the flapwise bending moment predictions, the first corresponding to the impulsive down-up loading in the normal loads data, the second trough occurring in the second quadrant as a result of negative sectional angles of attack. With increase in advance ratio, compressibility effects become more prominent on the advancing blade, giving rise to the corresponding waveform in the flapwise bending moment predictions. The flapwise bending moments are slightly under-predicted by CFD/CSD predictions. A consistent phase difference is observed between the measurement and the predictions.

The oscillatory torsional moment predictions show strong 4P variation at  $\mu = 0.15$ , which has not been captured accurately in CFD/CSD predictions. As advance ratio increases, the waveform for torsional moments is well-captured on the advancing side, while the sharp drop in torsional moment on the retreating side near  $\psi = 250^\circ$  is not well-predicted. The peak-to-peak magnitude is well-predicted. The prediction quality of oscillatory torsional moments is directly related to that of sectional pitching moments.

The test data for oscillatory chordwise bending moment at 40%R shows high frequency content at  $\mu = 0.15$ . The peak-to-peak of chordwise bending moment is significantly under-predicted and the phase is not well-captured. The correlation quality does not improve with increase in advance ratio.

The comparison of measured vs. predicted time histories of push-rod loads has been shown in Fig. 10 for the speed-sweep conditions. The advancing side wave-form is captured well while the dual-peak behavior on the retreating side is not well-captured.

#### E. Integrated Performance Results

The non-dimensional predicted performance indicators for thrust, propulsive force, power coefficient and lift to equivalent drag obtained from the coupled CFD/CSD analysis are compared against the test data for the parametric speed sweep in Fig. 11. The solution domain from where the performance indicators were extracted (CFD or CSD) is indicated in the legend. The CFD/CSD methodology employed performs well in predicting the integrated performance indicators as a function of advance ratio. The prediction of thrust is within experimental error limits, which is expected since thrust is one of the trim targets. The small differences between CFD and CSD predictions is due to interpolation effects not accounting for force conservation at the fluid and structure interface. The measured and predicted power coefficients compare well for all advance ratios. The agreement between predicted and measured propulsive force for the parametric speed sweep is good at lower advance ratios, while there is an over-prediction at higher advance ratios. Since the propulsive force is over-predicted at higher advance ratios, the  $L/D_e$  is over-predicted as well. Note that the use of fully turbulent flow, an assumption made in the current CFD methodology, tends to over-predict the viscous drag and may affect the stall behavior.

#### F. Correlation quality of airloads

In order to find out the correlation quality of predicted airloads with measured data, the statistical metric introduced by Bousman and Norman<sup>20</sup> was used for the parametric speed sweep. Makinen *et al.*<sup>21</sup> used this method to characterize the prediction quality of harmonic components of pushrod loads for a velocity sweep of flight conditions for the UH-60A Airloads Flight Test Data. A linear regression curve-fit of the data points provides three quantitative attributes of the correlation quality – slope ( $m$ ), coefficient of determination ( $r^2$ ) and vertical axis offset ( $b$ ). This metric can be used to study the improvement and degradation of the airloads prediction as a function of advance ratio. As the correlation quality improves, the slope ( $m$ ) and co-efficient of determination  $r^2$  approach unity. Fig. 12 shows correlation quality for sectional normal loads and pitching moments for the highest and the lowest advance ratio simulations carried out in this study. In general, the sectional normal loads were found to have the best correlation, while the correlation quality of pitching moments improves with increase in advance ratio. For  $\mu = 0.15$ ,

the correlation of pitching moments at  $r/R = 0.775$  and  $r/R = 0.4$  is the least. The best correlation in pitching moments is obtained at  $r/R = 0.92$  at this advance ratio. With increase in advance ratio, the correlation trends improve.

#### IV. Parametric Thrust Sweep

Results have been obtained for parametric thrust sweep conditions as tabulated in Table 2. These conditions range from an un-stalled condition to deeply stalled conditions. The parametric thrust sweep was carried out at a fixed  $\mu = 0.3$  and a constant tip Mach number  $M_{tip}$  of 0.625.

Run*	Data Point	$C_T/\sigma$	Corrected shaft angle of attack (deg)
45	28	0.020	0.15
45	29	0.040	0.31
45	30	0.060	0.47
45	33	0.090	0.70
45	36	0.120	0.94
45	40	0.123	0.97

**Table 2.** Wind-tunnel test database comprising of thrust-sweep conditions at  $\mu = 0.3$  (Ref. 2)

##### A. Blade root motion

Figures 13 a-c show comparison of measured and predicted collective, longitudinal and lateral cyclic angles. For the same forward speed, increase in blade loading results in increase in the rotor collective. The measured and predicted collective angles compare very well. There is good agreement between measured and predicted longitudinal cyclic angles for the thrust sweep. The lateral cyclic angle is over-predicted by the CFD/CSD analysis by a marginal amount, as seen in Fig. 13 c.

##### B. Sectional Airloads

The contour plots of predicted sectional normal loads and pitching moments for 3 thrust conditions  $C_T/\sigma = 0.02$ , 0.06 and 0.12 are shown in Fig. 14. The distribution of sectional normal force and pitching moments for the thrust sweep is significantly different from that of the speed sweep (Fig. 7). Since the rotor is operating at  $\mu = 0.3$ , compressibility effects on the advancing blade tip are observed for all the blade loading values in the parametric thrust sweep. At  $C_T/\sigma = 0.02$ , negative loading is observed through out the advancing side in both the normal sectional loads and pitching moments. As the blade loading value increases, the reverse flow region on the retreating side becomes pronounced as seen in normal loads data in Figs 14 b and c. At  $C_T/\sigma = 0.12$ , the pitching moment prediction shows two distinct stall regions on the retreating side. These regions are spread over a narrow range of azimuth and are characteristic of dynamic stall phenomena. The normal sectional loads at this blade loading value show four distinct areas of high lift.

Detailed sectional normal loads and pitching moment predictions at 92% radial station for the same 3 representative thrust sweep conditions is shown in Fig. 15. For the thrust sweep runs, the shaft angle of attack  $\alpha$  is very close to zero. The measured as well as predicted data show negative normal loads at 92% spanwise station on the advancing side. In Fig. 15, at  $C_T/\sigma = 0.06$ , BVI-induced pulses in the first quadrant are observed, similar to speed-sweep condition at  $\mu = 0.15$  (Fig. 8). The current methodology is able to capture the impulsive pitching moment variation in the first quadrant at  $C_T/\sigma = 0.06$ . There is a phase difference observed in the sectional normal loads on the advancing blade at this radial station. At higher thrust values, dynamic stall sets in and is clearly observed in the pitching moment data at  $\psi = 290^\circ$  and  $\psi = 340^\circ$ . The first dynamic stall cycle has been predicted accurately in magnitude and phase, while there is under-prediction in magnitude of the second dynamic stall at  $C_T/\sigma = 0.12$ . The stall cycles were observed only at blade loading values equal to and greater than 0.12.

##### C. Structural Loads

The structural loads for the thrust sweep runs are shown in Fig. 16. The peak-to-peak predictions of flapwise bending moment for the 3 representative thrust sweep runs compare well with the test data. At  $C_T/\sigma = 0.02$  and 0.06, the flapwise bending moment at 40%R shows high frequency oscillations near the end of the first quadrant and the beginning of the second. At  $C_T/\sigma = 0.12$ , the torsional moments prediction captures the waveform of the test data associated with dual dynamic stall on the retreating side. There is significant under-prediction of chordwise bending

moment at all values of  $C_T/\sigma$ . The CFD/CSD predictions show significant 5P oscillations manifesting as a result of dynamic stall events. The blade 2<sup>nd</sup> chord frequency is 4.69P and first torsion frequency is 4.53P, therefore, the structural response due to 5P aerodynamic forcing function as a result of dynamic stall is magnified.<sup>16</sup>

Figure 17 shows oscillatory push-rod loads for all the test conditions studied in the thrust sweep. The waveform of the push-rod loads is similar to the waveform of the torsion moments at  $r/R = 0.4$ . The peak-to-peak loads are well-predicted at lower blade-loading values. As the blade-loading increases, the magnitude of compressive push-rod loads on the retreating blade is magnified in the CFD/CSD predictions, due to stall effects.’

#### D. Integrated Performance Results

Figure 18 shows performance indicators for the measured and simulated thrust sweep conditions. The agreement between measured and predicted thrust coefficient values is excellent, since the rotor is trimmed to the specified thrust target. The power coefficient increases steeply with increase in blade loading value. There is a slight over-prediction in the power predictions. At low blade-loading values, the propulsive force coefficients are over-predicted for the parametric thrust-sweep. However, the lift to equivalent drag prediction matches the test-data. The equivalent drag is obtained by subtracting propulsive power from the total power. Since there is an over-prediction in both, the values of equivalent drag match well with the test data giving rise to a decent agreement in the  $L/D_e$  ratio.

#### E. Correlation quality of airloads

The statistical metric introduced by Bousman and Norman discussed in section IV-E, is applied to the lowest and highest blade loading conditions in order to determine the quality of correlation of predicted airloads with the measured data. Fig. 19 shows that correlation quality of both normal loads and pitching moments improves with increase in blade loading. At 77.5%R, the correlation of pitching moments is observed to be unsatisfactory because of the presence of trim tab at this location.

### V. Conclusions and Recommendations

Two parametric runs namely speed sweep at constant lift and thrust sweep at constant advance ratio were investigated for full-scale wind tunnel UH-60A rotor using a Hybrid CFD methodology and a multi-body dynamics CSD approach using loosely coupled CFD/CSD methodology. All the fundamental flow phenomena have been modeled by the current CFD/CSD methodology. The following are the key conclusions from the study.

#### *Speed Sweep*

1. The prediction of airloads at low advance ratio was found to be sensitive to the wake modeling effects. The multiple span wake model was found to be better in predicting impulsive loading arising due to blade-vortex interaction on the advancing and retreating sides. For accurately capturing the impulsive loading due to blade and vortex interactions using hybrid CFD methodology, embedded grids to ensure less dissipation of the near-wake may be used.
2. Best agreement in structural load prediction was obtained for flapwise bending moment data, followed by torsional moments. Torsional moments for  $\mu = 0.15$  show a strong 4P variation. While the peak-to-peak values of pushrod loads are captured, the retreating side waveform was not well-predicted. The retreating-side behavior needs to be further investigated.
3. The integrated performance results showed best agreement between measured and predicted thrust and power coefficients. The propulsive force agreement was found to be better at lower advance ratios while it was over-predicted at higher advance ratios. The equivalent lift to drag ratio was over-predicted at high advance ratios.
4. The trim control settings – collective, longitudinal cyclic are well predicted for the speed sweep, while lateral cyclic was consistently over-predicted by  $1^\circ$  to  $1.5^\circ$  at the most, for the parametric speed sweep.

#### *Thrust Sweep*

1. The test condition with  $C_T/\sigma = 0.06$  is characterized by BVI impulses seen on the advancing blade. At  $C_T/\sigma = 0.12$ , dynamic stall phenomena is seen on the retreating side. There is a slight over-prediction in the magnitude of normal loads.
2. The peak-to-peak and waveform of flapwise bending moment and torsional moments have been predicted moderately well. The 5P variation in the predictions for chordwise bending moment is amplified due to the dynamic stall events. The chordwise bending moments are under-predicted and phase is not well-matched.



3. The integrated results showed reasonable agreement in thrust coefficients, while an over-prediction in the power and propulsive force coefficients was observed. At lower blade-loading values, the percentage error in the prediction of propulsive force was found to be higher.
4. The trim control settings – collective, longitudinal cyclic as well as the lateral cyclic angles are captured consistently for the thrust sweep.

### Acknowledgments

This work was funded by the Vertical Lift Consortium, formerly the Center for Rotorcraft Innovation and the National Rotorcraft Technology Center (NRTC), U.S. Army Aviation and Missile Research, Development and Engineering Center (AMRDEC) under Technology Investment Agreement W911W6-06-2-0002, entitled National Rotorcraft Technology Center Research Program. The authors would like to acknowledge that this research and development was accomplished with the support and guidance of the NRTC and VLC. The views and conclusions contained in this document are those of the authors and should not be interpreted as representing the official policies, either expressed or implied, of the AMRDEC or the U.S. Government. The U.S. Government is authorized to reproduce and distribute reprints for Government purposes notwithstanding any copyright notation thereon.

### References

- <sup>1</sup>Bousman, W. G., and Kufeld, R. M., “UH-60A Airloads Catalog,” NASA-TM-2005-212827, AFDD/TR-05-003, Aeroflightdynamics Directorate (AMRDEC), U.S. Army Research, Development, and Engineering Command, Ames Research Center, Moffet Field, California, August 2005.
- <sup>2</sup>Norman, T. R., P. Shinoda, R. L. Peterson, and A. Datta. “Full-Scale Wind Tunnel Test of The UH-60A Airloads Rotor,” *Proceedings of the American Helicopter Society 67<sup>th</sup> Annual Forum*, Virginia Beach, VA, May 3-5, 2011.
- <sup>3</sup>Tung, C., Caradonna, F. X., and Johnson, W. R., “The Prediction of Transonic Flows on an Advancing Rotor,” *Proceedings of the American Helicopter Society 40<sup>th</sup> Annual Forum*, Arlington, VA, May 1984.
- <sup>4</sup>Rajmohan, N., “Application of Hybrid Methodology to Rotors in Steady and Maneuvering Flight,” Ph.D. Dissertation, School of Aerospace Engineering, Georgia Institute of Technology, Atlanta, GA, 2010.
- <sup>5</sup>Bauchau, O. A., “Computational schemes for flexible, nonlinear multi-body systems.” *Multibody System Dynamics*, Vol. 2 1998, pp. 169-225.
- <sup>6</sup>Potsdam, M., Yeo, H., Johnson, W., “Rotor Aerodynamic Prediction using Loose Aerodynamic and Structural Coupling,” *Proceedings of the American Helicopter Society 60<sup>th</sup> Annual Forum*, Baltimore, MD, June 2004.
- <sup>7</sup>Datta, A., Chopra, I., “Validation and Understanding of UH-60A Vibratory Loads in Steady Level Flight,” *Journal of the American Helicopter Society*, Vol. 49, No. 3, 2004, pp. 271-287.
- <sup>8</sup>Datta A., Sitaraman J., Chopra I., Baeder J. D., “CFD/CSD Prediction of Rotor Vibratory Loads in High-Speed Flight,” *Journal of Aircraft*, Vol. 43, No. 6, 2006, pp. 1698-1709.
- <sup>9</sup>Biedron R.T., Lee-Rausch E.M., “An Examination of Unsteady Airloads on a UH-60A Rotor: Computation versus Measurement,” *Proceedings of the American Helicopter Society 68<sup>th</sup> Annual Forum*, Fort Worth, TX, May 1-3, 2012.
- <sup>10</sup>Rajmohan, N., Manivannan, V., Sankar, L., Costello, M., and Bauchau, O.A., “Development of a Methodology for Coupling Rotorcraft Aeromechanics and Vehicle Dynamics to Study Helicopters in Maneuvering Flight,” *Proceedings of the American Helicopter Society 65<sup>th</sup> Annual Forum*, Grapevine, Texas, May 27 - 29, 2009.
- <sup>11</sup>Rajmohan N., Sankar L.N., Costello M., “Effect of Inflow Model on Coupling between Aeromechanics and Flight Mechanics,” *49<sup>th</sup> AIAA Aerospace Sciences Meeting*, Orlando, Florida, Jan 2011.
- <sup>12</sup>Rajmohan N., Marpu R., Sankar L.N., Baeder J.D., Egolf T. A., “Improved Prediction of Rotor Maneuvering Loads using a Hybrid Methodology,” *Proceedings of the American Helicopter Society 67<sup>th</sup> Annual Forum*, Virginia Beach, VA, May 3-5, 2011.
- <sup>13</sup>Marpu R., Sankar L.N., Makinen S., Baeder J.D., Egolf T. A., Wasikowski M., “Physics Based Modeling of Maneuver Loads for Rotor and Hub Design,” *American Helicopter Society Specialist’s Design Conference*, San Francisco, CA, Jan. 23-25, 2012.
- <sup>14</sup>Marpu R., Sankar L.N., Stephen M., Baeder J.D., “Computational Modeling of Diving-turn Maneuvers using Hybrid Methodology,” *Proceedings of the American Helicopter Society 68<sup>th</sup> Annual Forum*, Fort Worth, TX, May 1-3, 2012.
- <sup>15</sup>Romander, E., Norman, T.R., Chang, I-Chung, “Correlating CFD Simulation with Wind Tunnel Test for the Full-Scale UH-60A Airloads Rotor,” *Proceedings of the American Helicopter Society 67<sup>th</sup> Annual Forum*, Virginia Beach, VA, May 3-5, 2011.
- <sup>16</sup>Yeo H., Romander E., “Loads Correlation of a Full-Scale UH-60A Airloads Rotor in a Wind Tunnel,” *Proceedings of the American Helicopter Society 68<sup>th</sup> Annual Forum*, Fort Worth, TX, May 1-3, 2012.
- <sup>17</sup>Bousman, William G. “A Qualitative Examination of Dynamic Stall from Flight Test Data.” *Journal of the American Helicopter Society*, Vol. 43, No. 4, 1998, pp. 279-295.
- <sup>18</sup>Kufeld, R.M., Bousman, W.G., “High Load Conditions Measured on a UH-60A in Maneuvering Flight,” *Journal of the American Helicopter Society*, Vol. 43, No. 3, 1998, pp. 202-211.

<sup>19</sup>Bhagwat, M. J., Ormiston, R. A., Saberi, H. A. and Hong, X., " Application of CFD/CSD Coupling for Analysis of Rotorcraft Airloads and Blade Loads in Maneuvering Flight," *Proceedings of the American Helicopter Society 63<sup>rd</sup> Annual Forum*, Virginia Beach, VA, May 1-3, 2007.

<sup>20</sup>Bousman W., and Norman T., "Assessment of Predictive Capability of Aeromechanics Methods," *Journal of the American Helicopter Society*, Vol. 55, No. 1, 2010, pp. 12.

<sup>21</sup>Makinen A.M., Wake B.E., Opoku D., "Quantitative Evaluation of Rotor Load Prediction Results Correlated to Flight Test Data", *Proceedings of the American Helicopter Society 67<sup>th</sup> Annual Forum*, Virginia Beach, VA, May 3-5, 2011.

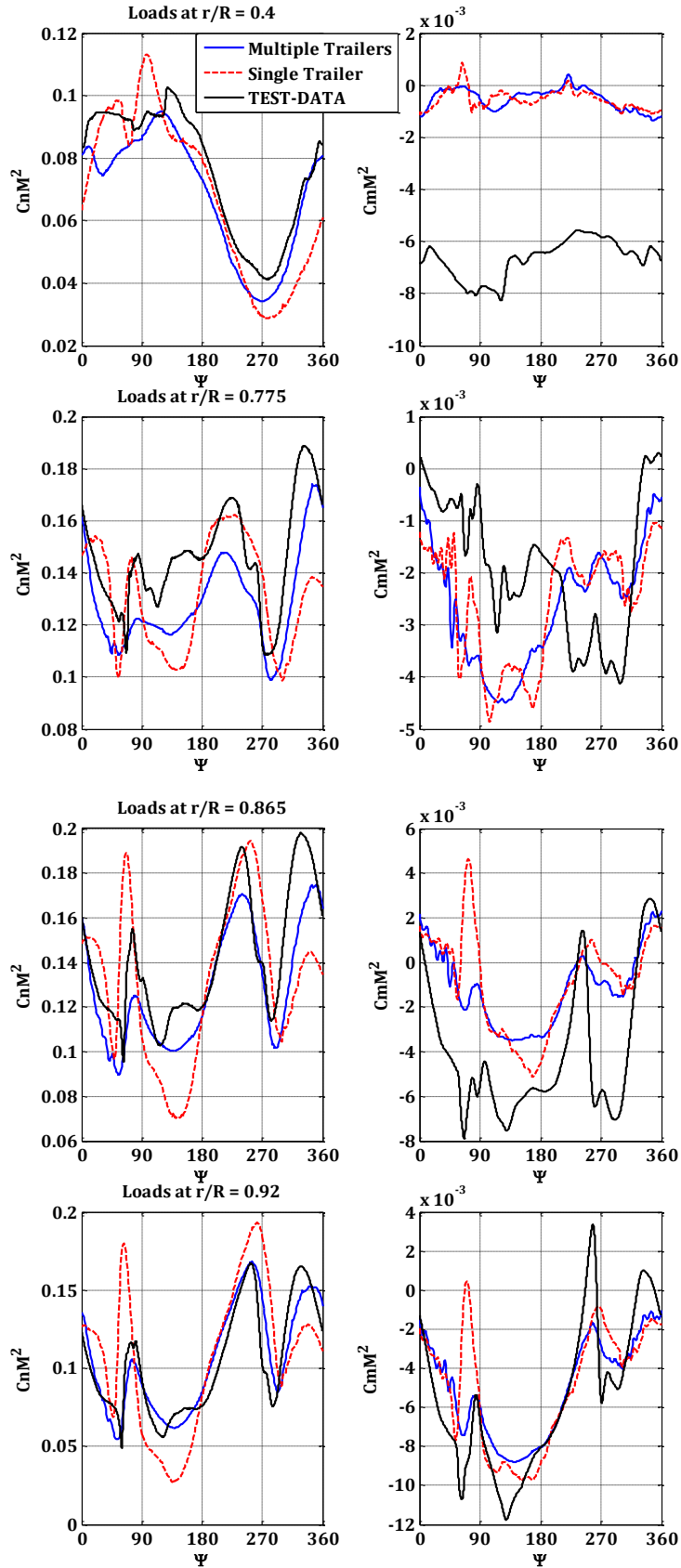
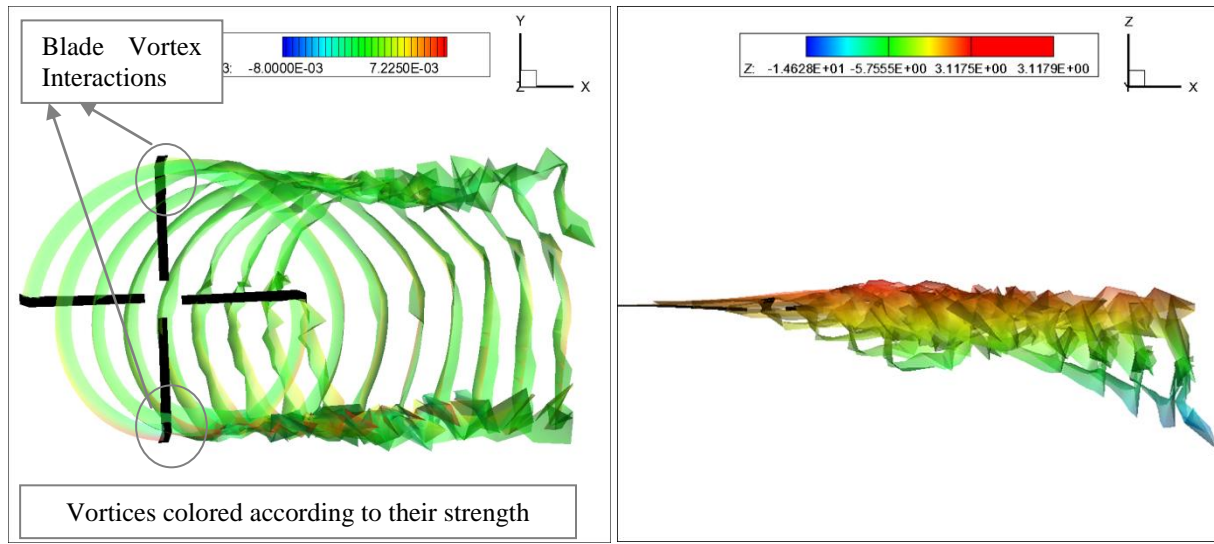


Figure 3. Sectional normal loads and pitching moments for Run 5215 with  $\mu = 0.15$ .



a) Tip vortices colored according to strength

b) Vortices colored according to vicinity from tip-path-plane

**Figure 4. Wake geometry obtained using Hybrid CFD methodology for  $\mu = 0.15$  condition. Only the vorticity near the tip region has been visualized for clarity.**

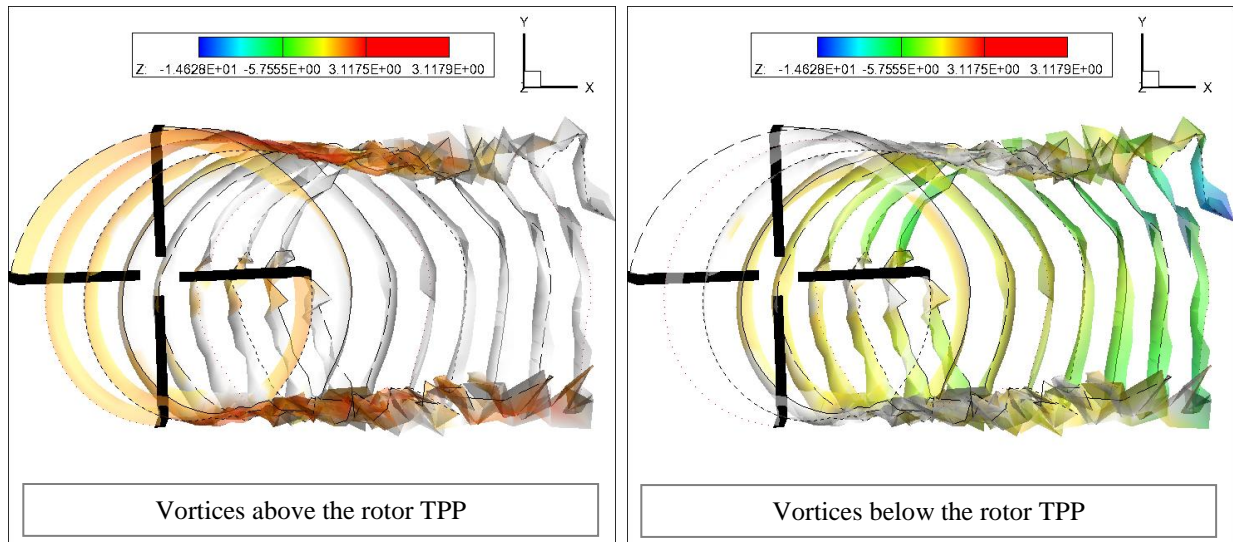


**Figure 5. Vortices above and below the rotor tip path plane at  $\mu = 0.15$  condition. Only the vorticity near the tip region has been visualized for clarity.**

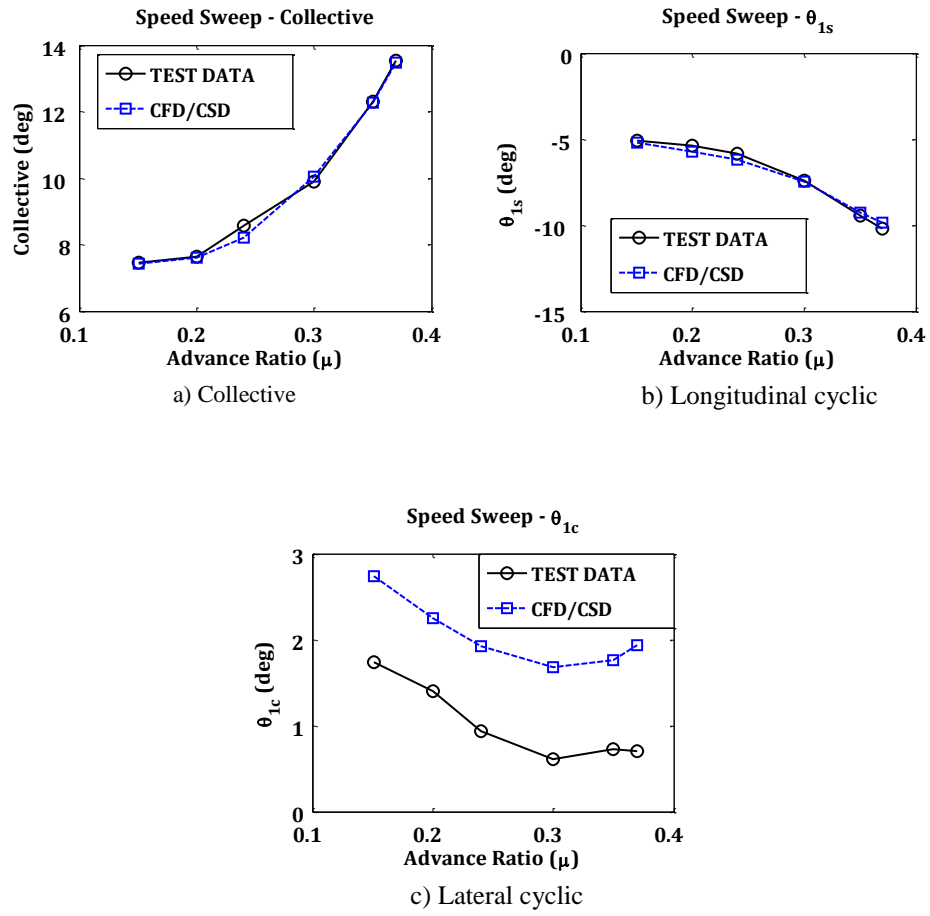
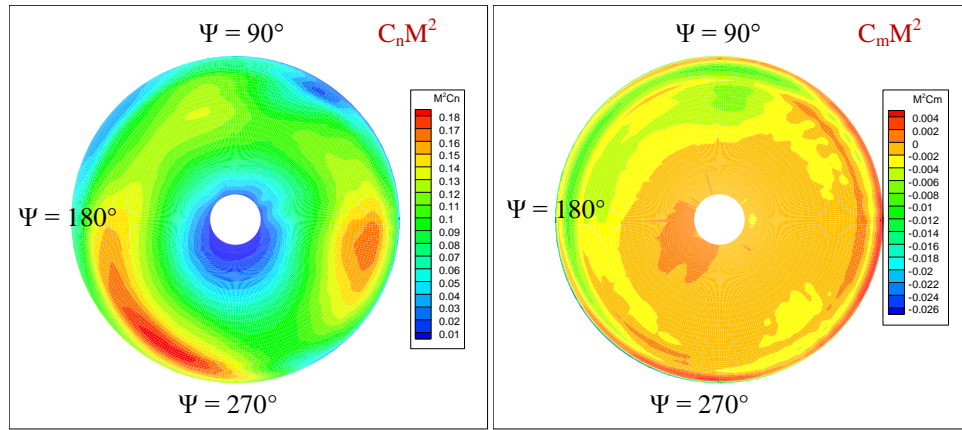
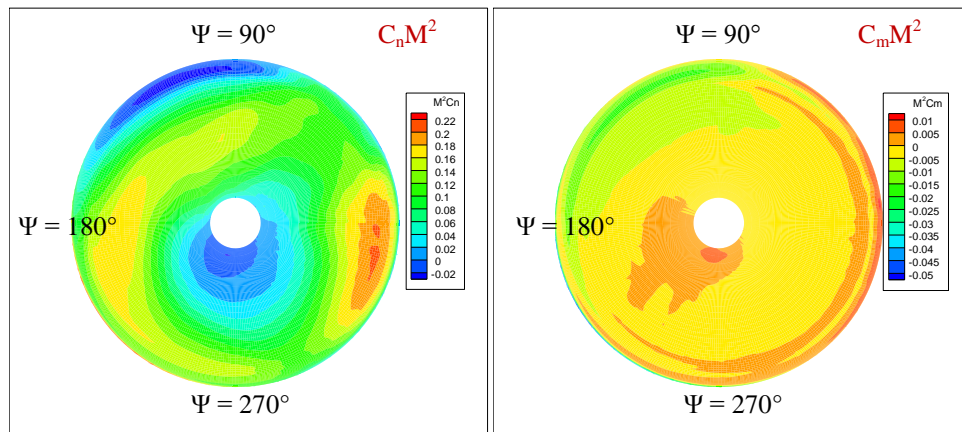


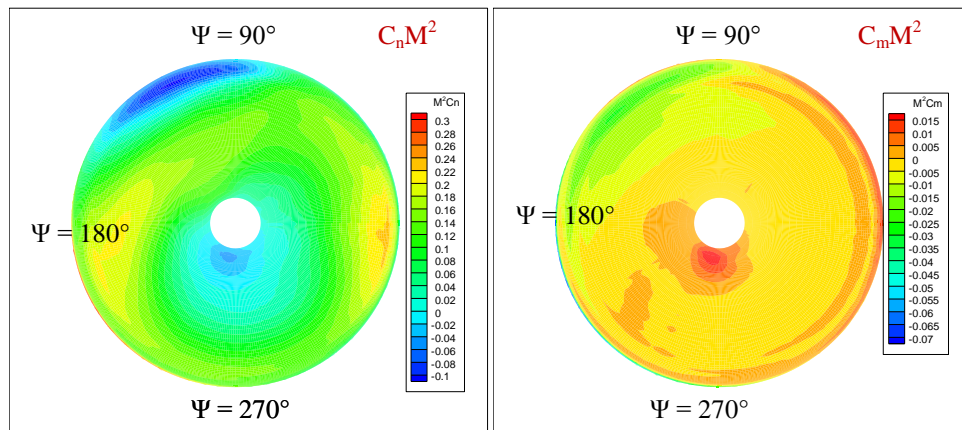
**Figure 6. Calculated and measured blade pitch angle for speed sweep.**



a)  $\mu = 0.15$ ,  $C_T/\sigma = 0.09$ , Test Run 5215



b)  $\mu = 0.3$ ,  $C_T/\sigma = 0.09$ , Test Run 5231



c)  $\mu = 0.37$ ,  $C_T/\sigma = 0.09$ , Test Run 5240

**Figure 7. Predicted sectional normal loads and pitching moments for selected speed sweep conditions.**

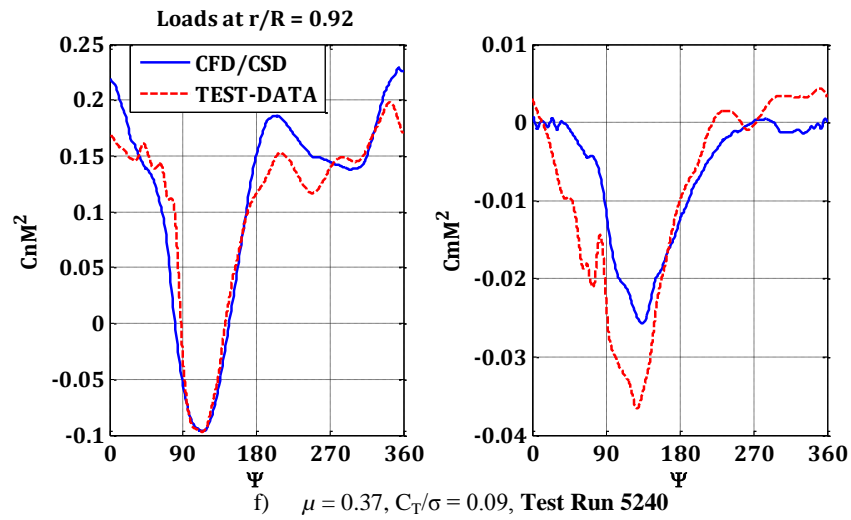
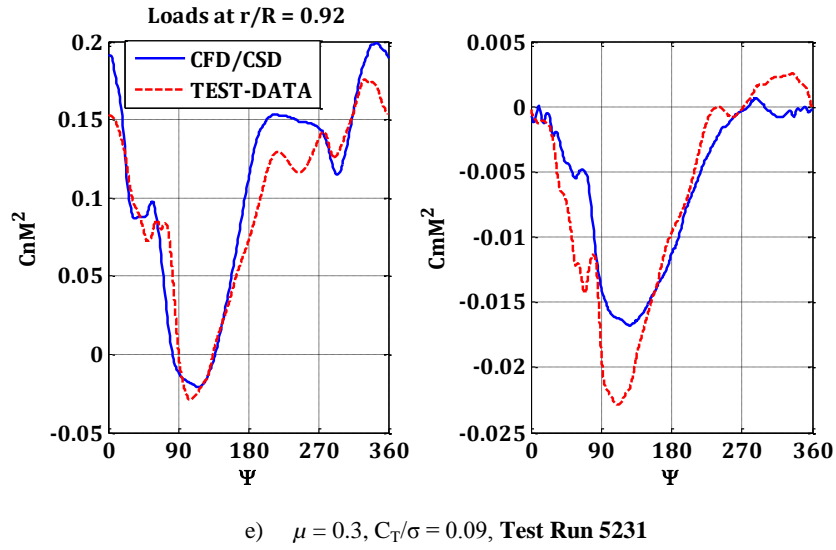
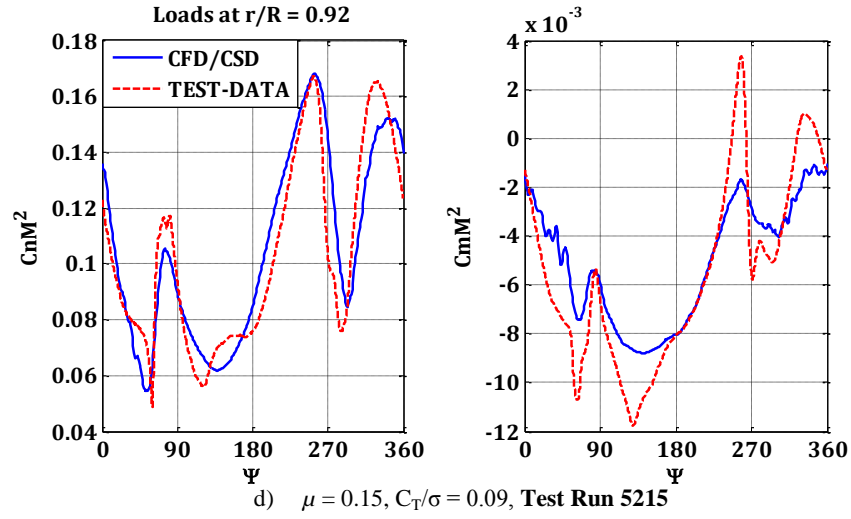
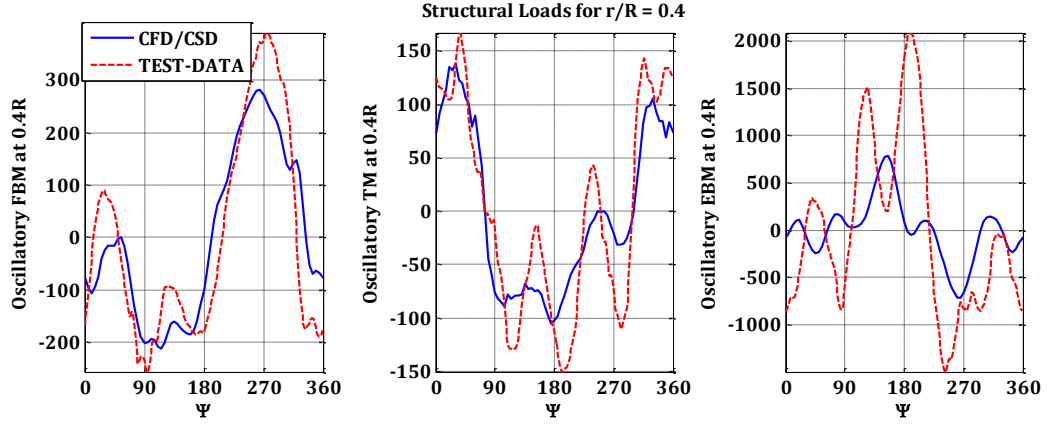
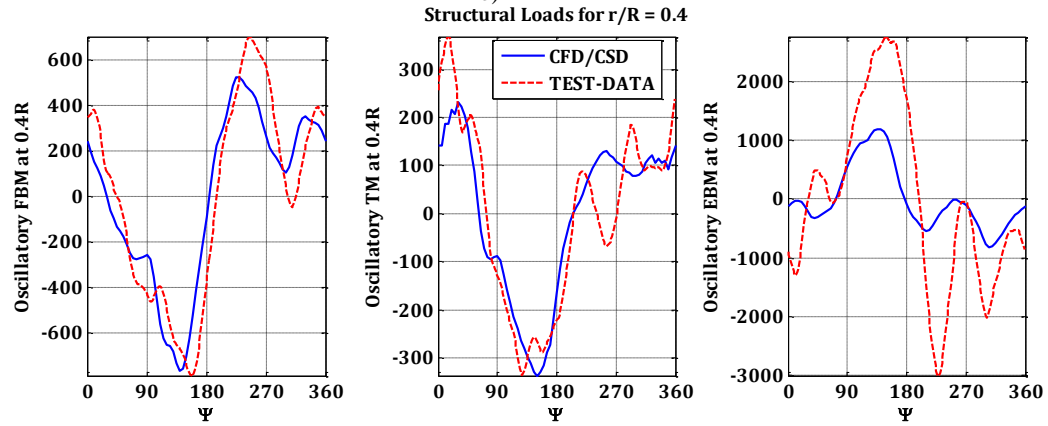


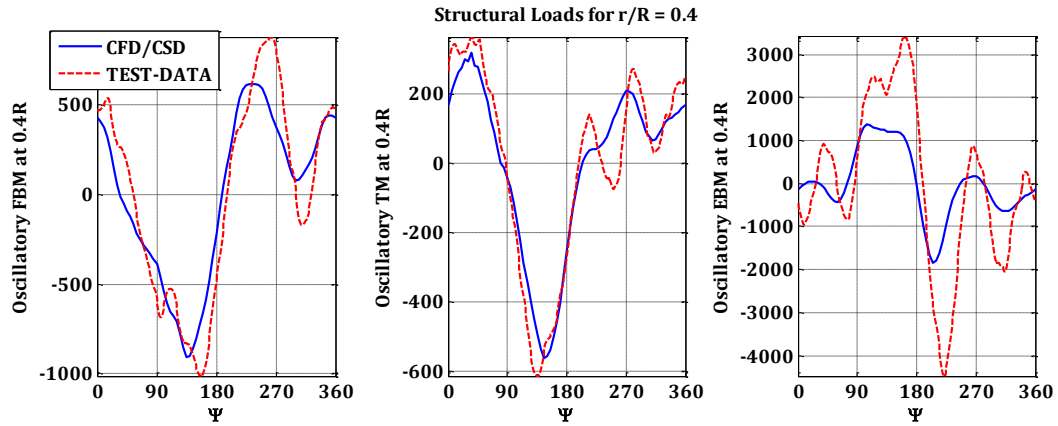
**Figure 8. Comparison of measured and predicted sectional normal loads and pitching moments at  $r/R = 92\%$ , for selected speed sweep conditions.**



a)  $\mu = 0.15$ ,  $C_T/\sigma = 0.09$ , Test Run 5215  
b)



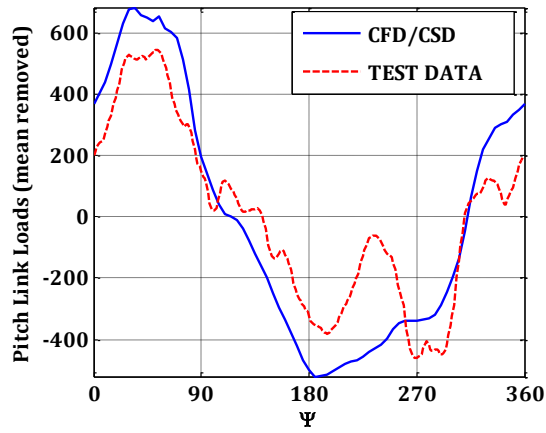
c)  $\mu = 0.3$ ,  $C_T/\sigma = 0.09$ , Test Run 5231



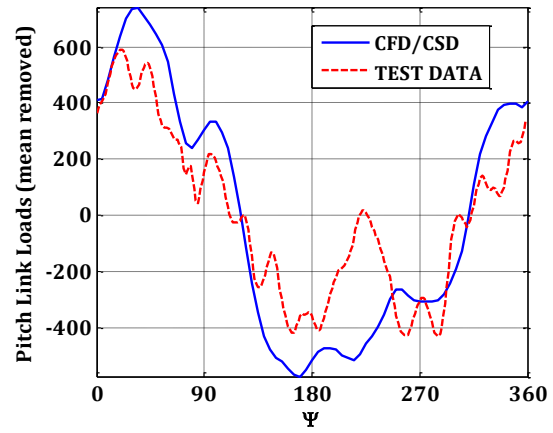
d)  $\mu = 0.37$ ,  $C_T/\sigma = 0.09$ , Test Run 5240

**Figure 9.** Comparison of measured and predicted blade oscillatory flapwise bending moment (FBM), torsional moment (TM) and edgewise bending moment (EBM) respectively at  $r/R = 40\%$  for selected speed sweep conditions.

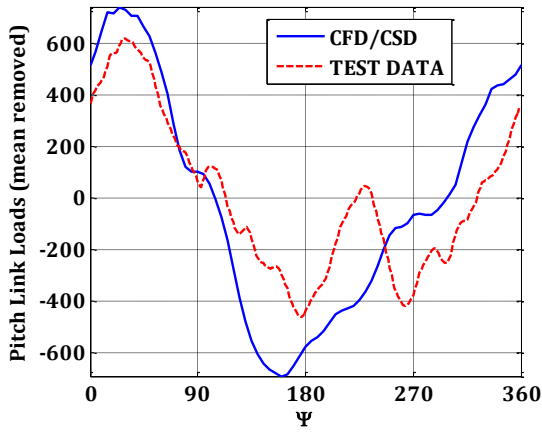




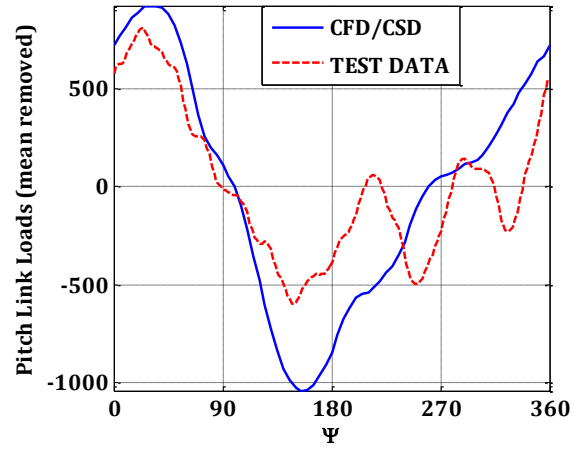
a)  $\mu = 0.15$ ,  $C_T/\sigma = 0.09$ , Test Run 5215



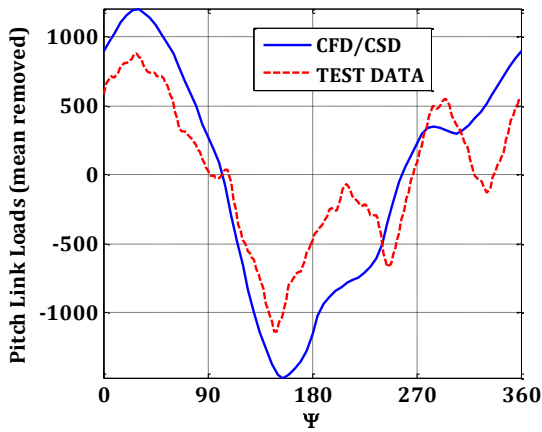
b)  $\mu = 0.2$ ,  $C_T/\sigma = 0.09$ , Test Run 5220



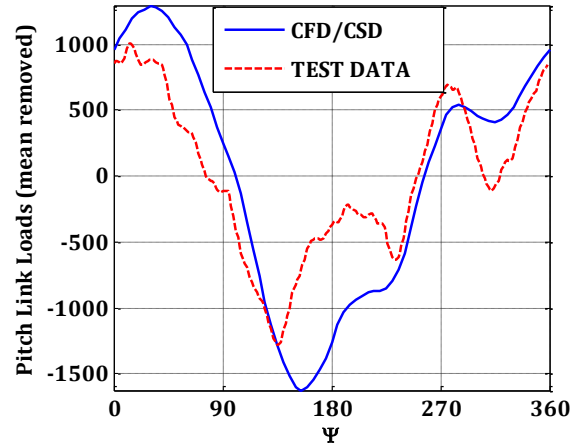
c)  $\mu = 0.24$ ,  $C_T/\sigma = 0.09$ , Test Run 5225



d)  $\mu = 0.30$ ,  $C_T/\sigma = 0.09$ , Test Run 5231



e)  $\mu = 0.35$ ,  $C_T/\sigma = 0.09$ , Test Run 5235



f)  $\mu = 0.37$ ,  $C_T/\sigma = 0.09$ , Test Run 5240

Figure 10. Comparison of measured and predicted blade oscillatory push rod loads for speed sweep conditions.

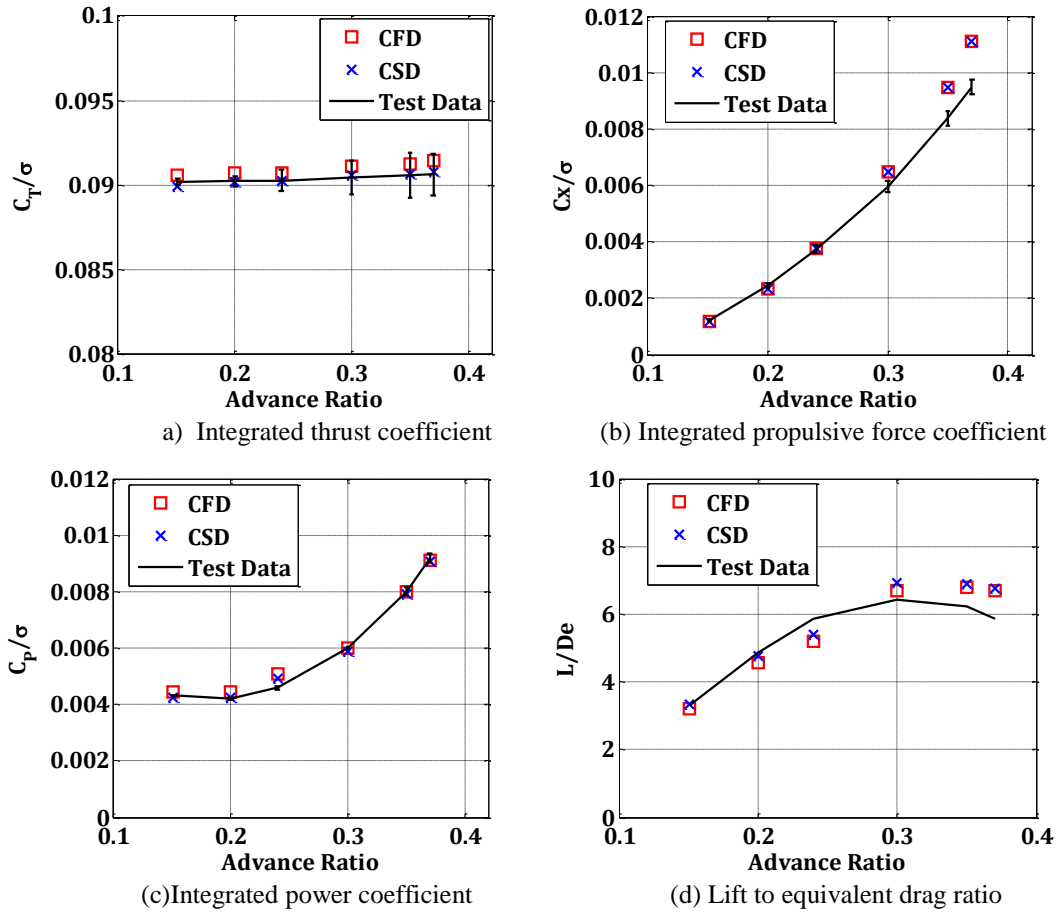


Figure 11. Performance indicators as a function of advance ratio.

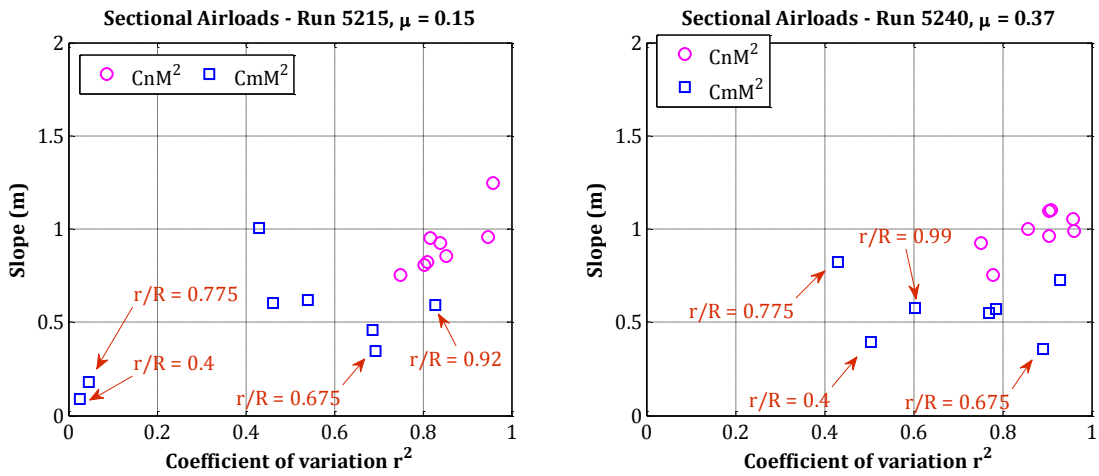
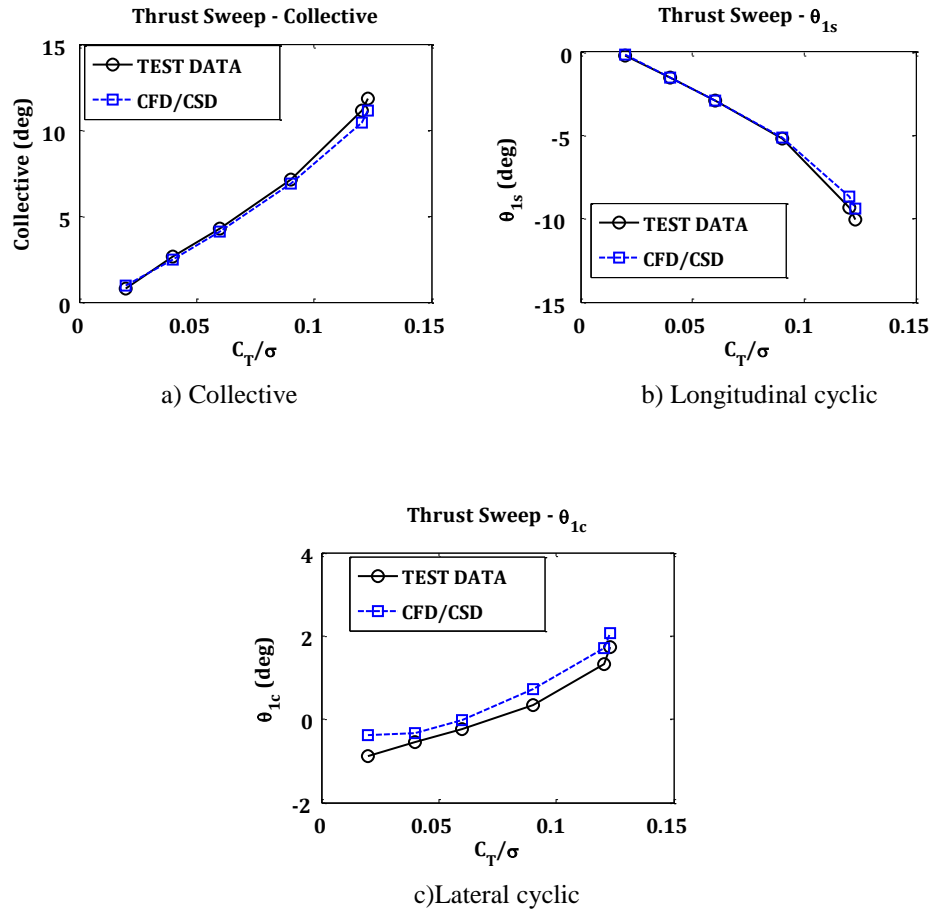
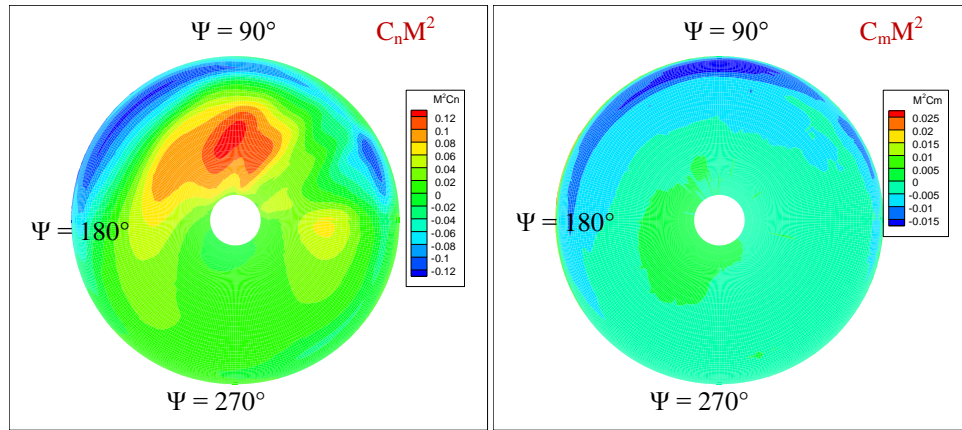


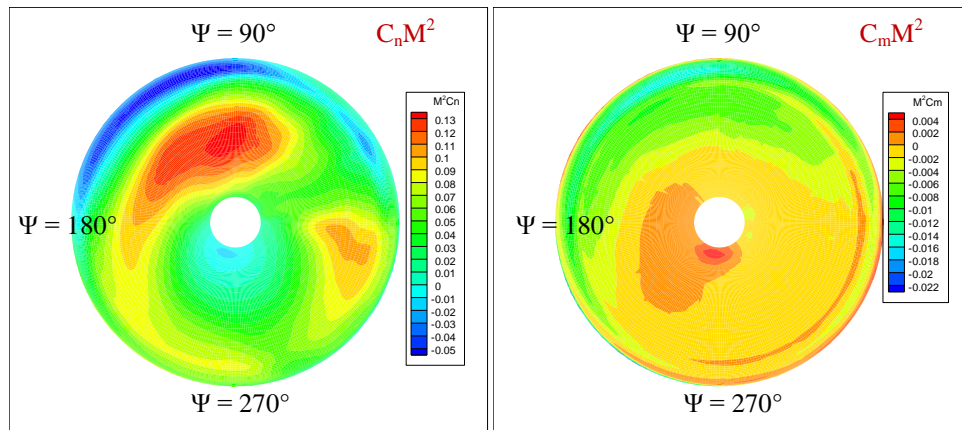
Figure 12. Prediction quality of sectional normal loads and pitching moments for 2 advance ratios  $\mu = 0.15$  and  $\mu = 0.37$ . Best correlation quality corresponds to  $m = 1$  and  $r^2 = 1$ .



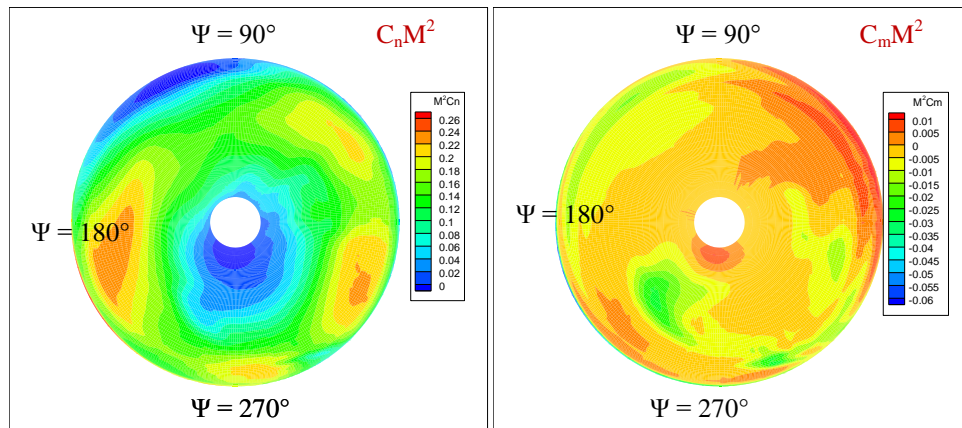
**Figure 13. Calculated and measured blade pitch angle for thrust sweep.**



a)  $C_T/\sigma = 0.02, \mu = 0.3$ , Test Run 4528



b)  $C_T/\sigma = 0.06, \mu = 0.3$ , Test Run 4530



c)  $C_T/\sigma = 0.12, \mu = 0.3$ , Test Run 4540

Figure 14. Predicted sectional normal loads and pitching moments for selected thrust sweep conditions.

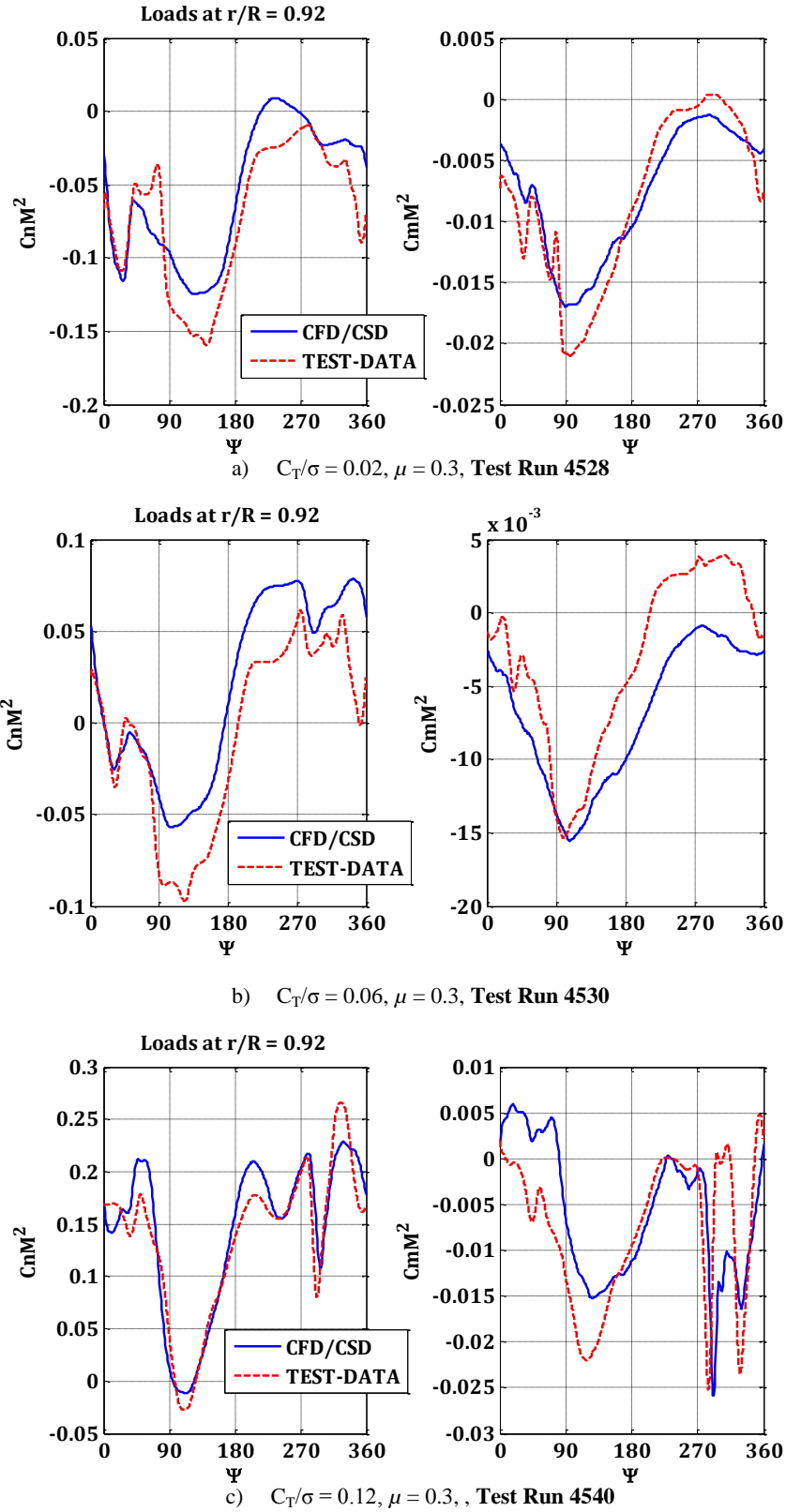


**Figure 15. Comparison of measured and predicted sectional normal loads and pitching moments at  $r/R = 0.92$ , for selected thrust sweep conditions.**

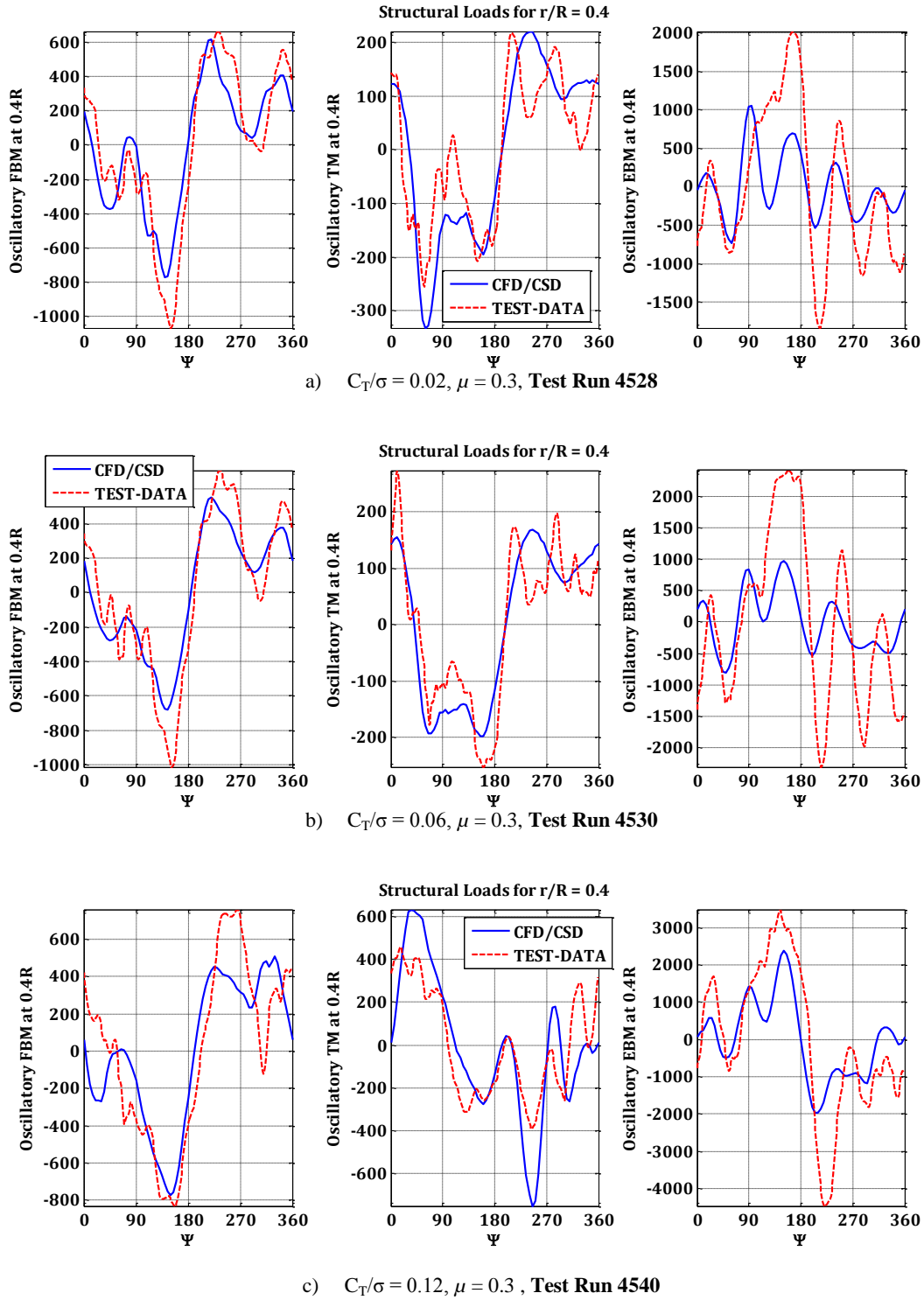
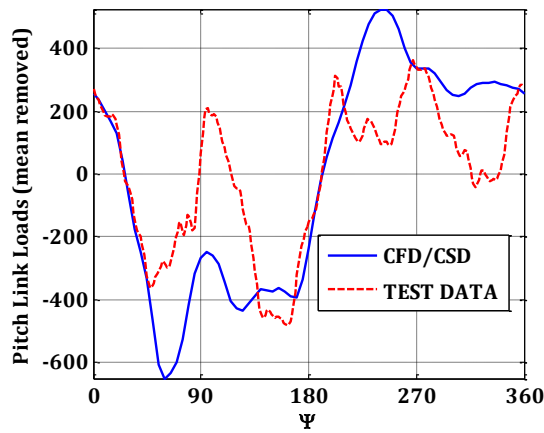
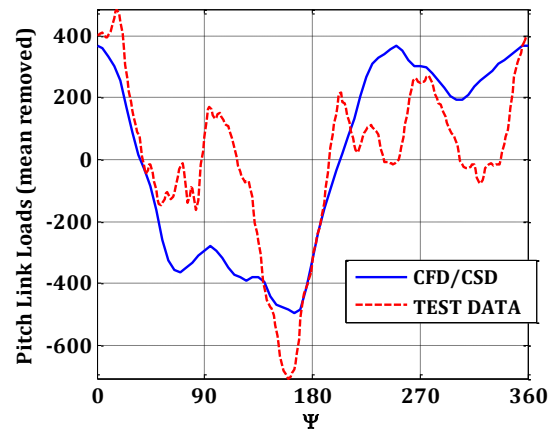


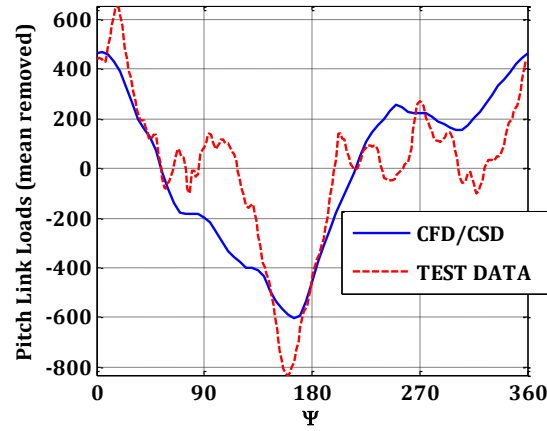
**Figure 16. Comparison of measured and predicted blade oscillatory flapwise bending moment (FBM), torsional moment (TM) and edgewise bending moment (EBM) respectively at  $r/R = 0.4$  for selected thrust sweep conditions.**



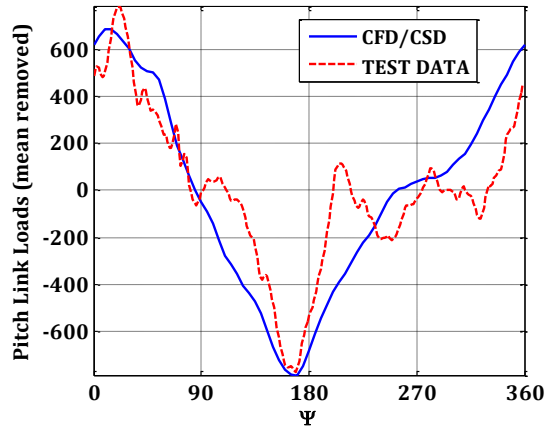
a)  $C_T/\sigma = 0.02, \mu = 0.3$  Test Run 4528



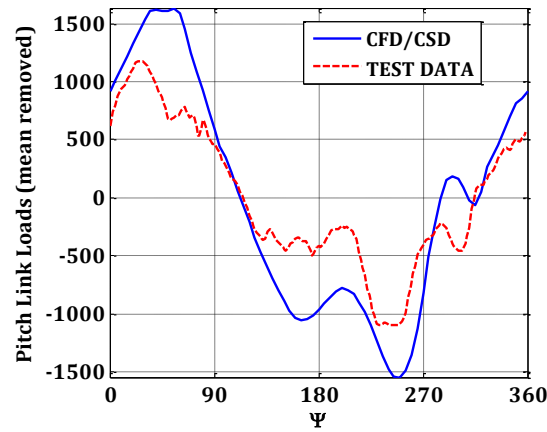
b)  $C_T/\sigma = 0.04, \mu = 0.3$ , Test Run 4529



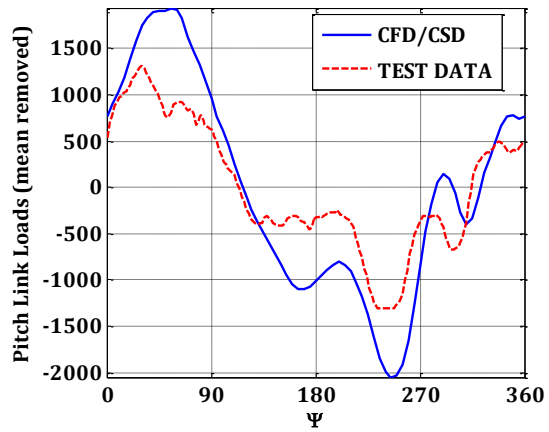
c)  $C_T/\sigma = 0.06, \mu = 0.3$ , Test Run 4530



d)  $C_T/\sigma = 0.09, \mu = 0.3$ , Test Run 4533



e)  $C_T/\sigma = 0.1203, \mu = 0.3$ , Test Run 4536



f)  $C_T/\sigma = 0.1231, \mu = 0.3$ , Test Run 4540

**Figure 17. Comparison of measured and predicted blade oscillatory push rod loads for thrust sweep conditions.**

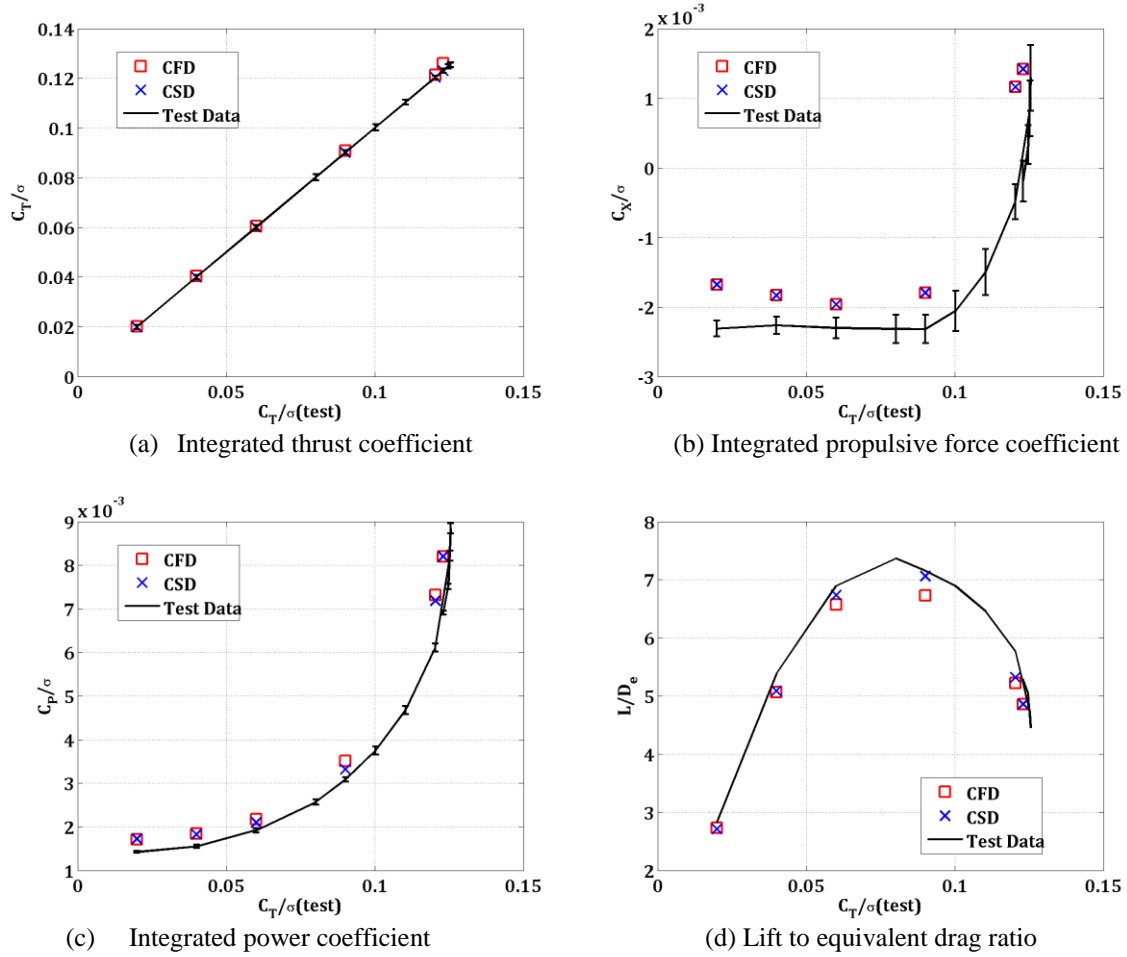


Figure 18. Performance indicators as a function of blade loading.

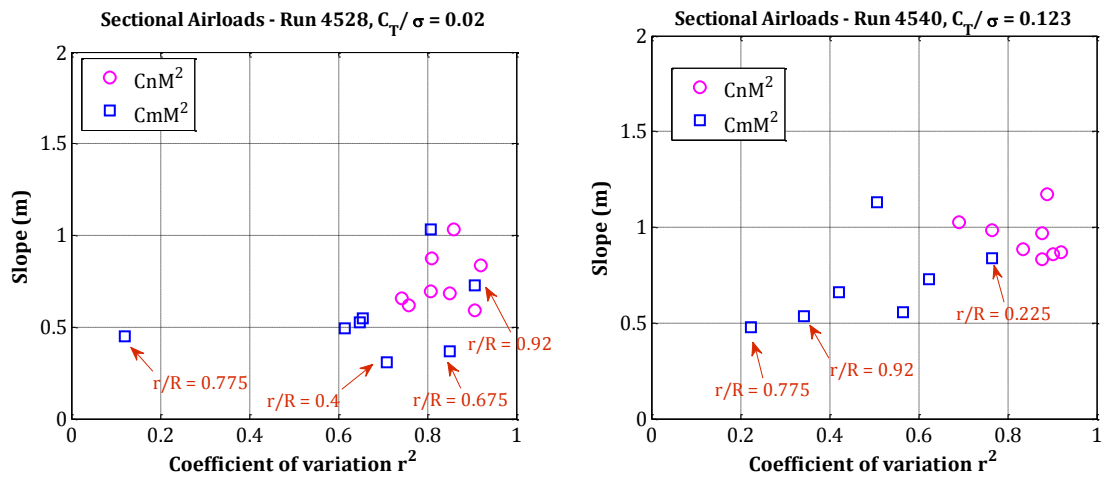


Figure 19. Prediction quality of sectional normal loads and pitching moments for 2 blade loading values,  $C_T/\sigma = 0.02$  and  $\mu = 0.12$ . Best correlation quality corresponds to  $m = 1$  and  $r^2 = 1$ .